ACCEPTED MANUSCRIPT

Probing the dynamics of water over multiple pore scales in cement by atomistic simulations

SM Mutisya, JM de Almeida, CR Miranda

Applied Surface Science, 895, 15, 115429 (2021)

DOI: https://doi.org/10.1016/j.apsusc.2021.150426

© 2021. This manuscript version is made available under the CC-BY-NC-ND 4.0 license https://creativecommons.org/licenses/by-nc-nd/4.0/. The final published version appeared in Applied Surface Science and is available at https://doi.org/10.1016/j.apsusc.2021.150426.

Probing the dynamics of water over multiple pore scales in cement by atomistic simulations

Sylvia M. Mutisya[a], James M. de Almeida[b], Caetano R. Miranda[b,*]

[a] *Nanociências e Materiais Avançados, Universidade Federal do ABC, Santo André, SP, 09210-580, Brazil*
[b] *DFMT, Instituto de Física, Universidade de São Paulo, São Paulo, SP, 05508-090, Brazil*

Abstract

The presence of water in hydrated cement has significant effects on the properties of concrete. However, direct correlation of water with the macroscopic properties of concrete remains a major challenge. In this study, we use molecular dynamics simulations to determine the water dynamical properties in four pore environments of the calcium silicate hydrate (C–S–H) colloid model; interlayer pores, gel pores, connected pores and in the vicinity of a finite disk–like globule particles. It was revealed that the translational and rotational dynamics are decoupled, consequently, the translational dynamics govern the calculated T_2 relaxation time at the surface. Based on NMR T_2–T_2 relaxation investigation, we showed an exchange between 1 and 4 nm connected pores. At short times, the adsorption/desorption of water from a 1 nm pore is limited to the edges, a behavior linked to water sorption hysteresis. The properties of water in the proximity of a finite C–S–H globule and confined in infinite pore models are comparable.

Keywords: Cement; Calcium Silicate Hydrate (C–S–H); Diffusion; T_2 Relaxation time; Molecular Dynamics

*Corresponding author
Email address: cmiranda@if.usp.br (Caetano R. Miranda)

1. Introduction

Cement is a widely used material in construction industry as a binder of concrete. The chemical reaction of anhydrous cement powder with water gives rise to a complex heterogeneous hydrated paste, with 50–70% constituted by calcium silicate hydrate (C–S–H, where C = CaO, S = SiO_2 and H = H_2O) [1]. The overall properties of concrete infrastructures are highly correlated to the presence of water in C–S–H [2–4]. To improve our current understanding of cement and its properties, it is therefore necessary to probe C–S–H over a broad scale. However, these efforts are constrained by the limited knowledge of C–S–H, whose exact atomistic structure is not yet known.

Several models of the C–S–H nanostructure have been proposed [5–8]. Particularly, Jennings colloid model–II (CM–II) [8] is universally accepted since it could reconcile several controversial data from the literature. According to the CM-II model, C–S–H is constituted by tiny globules of sizes ranging from 3 to 15 nm and a morphology that experiments suggest can be spherical, elliptical, disk–like or lamellar [8–10]. These globules assemble to form the pore network of C–S–H, consisting of interlayer and intraglobular pores ($<$ 1 nm), small gel pores (1–3 nm), large gel pores (3–12 nm) and capillary pores ($>$ 12 nm).

Water in each pore category strongly impacts the fluid transport and mechanical properties of cement. For instance, water within sub-nanometer pores has implications on drying shrinkage hysteresis [2] while small gel pores have been associated with the shrinkage and creep mechanisms [3, 4]. Additionally, depending on the local environment, water molecules in C–S–H can promote a disjointing behavior or enhance the cohesion within and between the C–S–H particles [11], with the loss of cohesion occurring for distances as small as 1 nm [11, 12]. Despite the several efforts to correlate nanoscale cement structure with engineering properties, no single model has been successful in capturing all the processes so far, and hence, the role of water in cement remains an area of active research.

To unravel the state of water within C–S–H, a variety of experimental tech-

niques have been utilized. For example, ^{1}H nuclear magnetic resonance (NMR) [13–15], quasi-elastic neutron scattering (QENS) [16, 17], differential scanning calorimetry [18], broadband dielectric spectroscopy [19] and Fourier transform infrared spectroscopy [18]. From the experimental point of view, this is however a very challenging task, and it is often difficult to interpret the data. Despite their inherent shortcomings, these studies have identified three relaxation components for water in cement paste. This has resulted in the categorization of water into either chemically bound, physically bound or 'free' bulk water [17, 19–22].

Atomistic simulations can provide valuable complementary information to aid in the interpretation of the experimental data of the nanostructure of C–S–H at the molecular level. For simulations at the nanoscale, it is commonplace to model water within C–S–H interlayer and gel pores by isolated infinite planar pores [23–26]. This approach ensures the study of water properties in contact with C–S–H basal surfaces, providing no information on the edge surfaces, water exchange, and the fact that C–S–H is constituted by nanometer–sized globules.

In this work, we employ molecular dynamics (MD) simulations to study the dynamical properties of water within the pore network of C–S–H, to provide molecular level insights as to the state of water within C–S–H. The pore geometry models built include infinite planar pores (used to model interlayer and gel pores), a connected pore model, and a finite pore space created by the arrangement of disk–like globule particles. These pore models allow us to investigate the consequences of the pore surface chemistry, confinement, connected pores and pore geometry on the measurable dynamical properties of water nanoconfined therein.

The effect of the C–S–H surface chemistry and nanoconfinement on water structure and dynamics is tackled using infinite planar pore models. A qualitative analysis of water exchange in connected C–S–H pores is performed using the connected pore model, bearing in mind that the exchange times measured experimentally [27] are beyond the limit of our atomistic simulations. Water exchange in connected nanopores is important as it is expected to influence

fluid and ion transport within concrete structures, which are key factors in the overall durability of concrete. Previous studies have reported water exchange in freshly hydrated cement pastes based on T_1–T_2 and T_2–T_2 NMR relaxation experiments [27]. Lastly, we study the state of water within the proximity of a globule—viewed as a first step towards upscaling. This allows exploration of water dynamics between finite parallel globules and within the edge–edge pore environment (pores between adjacent edges of the globule particles), which is largely unknown. Despite a few studies [28–30] on the cohesive, normal and frictional forces between individual globule particles using MD simulations, the particulate nature of C–S–H remains evident only in investigations at the mesoscale [31–33].

The C–S–H nanostructure is based on the CM-II model [8], with the atomic structure modeled using a defected tobermorite structure. The timescale of the water dynamics explored ranges from subfemtosecond to tens of nanoseconds. Within this timescale, we could distinguish the dynamics of water into fast and slow processes. The fast processes taking place at the femtosecond timescale are quantified by infrared spectra from the vibrational density of states (VDOS). The slow processes, on the other hand, are determined by self–diffusion coefficient, rotational correlation times, residence times, exchange times and NMR T_2 relaxation times. The exchange of water in different pores is investigated by implementing 2D T_2–T_2 NMR relaxation [27, 34].

2. Methods

2.1. The atomistic C-S-H models

Following the existing experimental information on C–S–H [35–37], a fully atomistic model of C–S–H was constructed starting from normal tobermorite 11 Å crystal [38]. To obtain a higher Ca/Si ratio, there are several procedures to introduce defects on crystalline tobermorite. In this work, the introduction of the defects follows the atomistic C–S–H model (model 1) reported by Kovačević et al. [39]. Firstly, the occupancy of the interlayer calcium atoms was doubled,

raising the Ca/Si ratio of the initial configuration from 0.75 for the tobermorite crystal to 0.83. The unit cell was then replicated (4×4×1) along a, b, and c crystallographic directions. All the connected double chains of silicate were removed by deleting SiO units, as according to NMR experiments [35], there are no cross-linked silicate chains (Q_3) in C–S–H. For every SiO unit removed, either O5 or O6 (O5 and O6 follows the notation used by Merlino et al. [38]) oxygen atom was passivated with hydrogen atoms to form Si–OH linkages. The H^+ atoms are added to the O5 or O6 sites to facilitate charge neutralization introduced by removal of SiO units, since the extra Ca^{2+} atoms introduced into our model by doubling the occupancy of interlayer Ca2 atoms, are not enough to neutralize the system. The resultant atomistic C–S–H model contains 9.6 % of Si–OH which lies within the experimental range of < 12 % for low C/S ratio C–S–H of < 1.35 [35].

To further increase the Ca/Si ratio, the infinite "dreierketten" silicate chains are broken by removal of charge neutral SiO_2 units randomly. Breaking the silicate chains creates additional non–bridging oxygen atoms which act as sites for hydrogen bonds. Hence, this process is expected to enhance the hydrophilic nature of our C–S–H model, stemming from the existence of surface OH groups and non-bridging oxygen atoms that could act as hydrophilic adsorption sites. The defected tobermorite structure was then transformed to its equivalent orthorhombic cell with lattice parameters $a = 45.08$ Å, $b = 29.48$ Å and $c = 22.68$ Å. The final structure (Figure 1 a)) has a Ca/Si ratio of 1.1 and the silicate chain lengths include dimers, pentamers and octamers, in line with the predominant chain lengths observed experimentally [35, 36].

With this structure, we have built different models for the C–S–H, as shown in Figure 1. The infinite planar interlayer and gel pores are described in subsection 2.1.1, the connected gel pore model in subsection 2.1.2, and the disk-like globule model in subsection 2.1.3.

2.1.1. Infinite planar interlayer and gel pores

The first pore environment considered in our simulations is infinite planar interlayer and gel pores. The interlayer pores are modeled by the interlayer region of the defected tobermorite model, while the gel pores are created by increasing the interlayer pore spaces to 1–5 nm (Figure 1 b)). For normal tobermorite 11 Å, the interlayer space lies along the (002) plane. The size of the interlayer pore is $\approx$ 0.6 nm; a typical size of two-layer pores in clays. After cleavage, the surfaces contain O atoms both protonated ($\equiv$Si–OH) and deprotonated (Si–O^-) groups and a distribution of Ca^{2+} cations and H_2O molecules originally belonging to the interlayer (see illustration of the (001) surface in Figure 1). Water at a density of 1 g/cm^3 was incorporated inside the gel pores with the PACKMOL software [40]. The number of water molecules within the planar pores is 160, 455, 910, 1365, 1820 and 2275 for an interlayer, 1, 2, 3, 4 and 5 nm pores respectively.

2.1.2. Connected gel pore model

Building on from the infinite slit pores, the connected pore model is constructed by further cleaving the defected tobermorite structure along the (100) direction to create a 4 nm pore perpendicular to the interlayer and the 1 nm pores (see Figure 1 c)). The (100) surface has been shown to be among the most stable facets of tobermorite polymorphs [41, 42]. This is justified since the silicate chains in tobermorite run along the [010] crystallographic direction (see an illustration of the silicate chains along the [010] crystallographic direction in Figure 1). Thus, cleaving along the (100) plane does not invoke any breaking of the Si–O bonds. The (100) surface consists of water molecules, calcium, and non-bridging oxygen atoms (see the zoomed out illustration in Figure 1). Such a pore system allows monitoring the transport of water along the a axis (the pore length is 90.15 Å) of the interlayer and the 1 nm small gel pore.

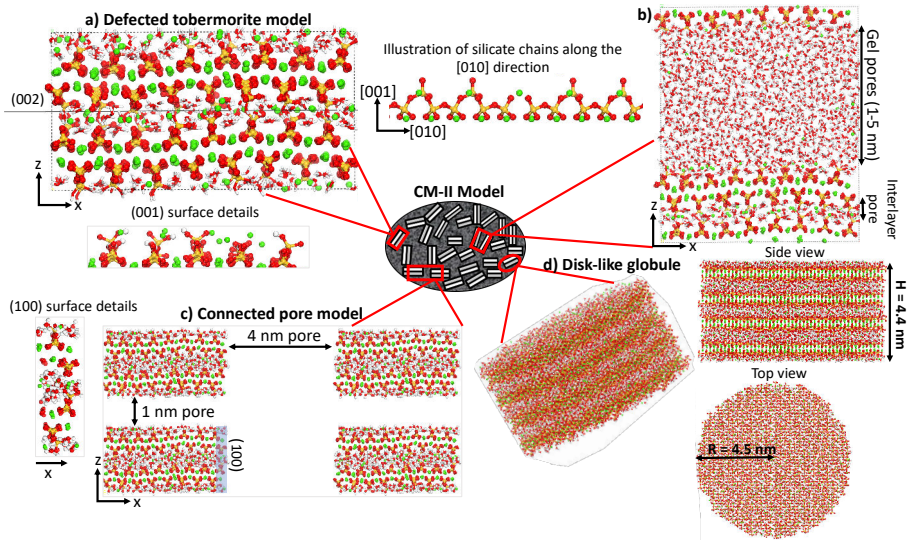

Figure 1: Pore models built following the Jennings CM-II model [8]. a) Illustration of the defected tobermorite C–S–H model building block and the position of the (002) cleavage plane. The surface details of the (001) surface and an illustration of the silicate chains running along the [010] crystallographic direction are shown in the zoomed out figures. The water molecules are removed for clarity. b) A model for the C–S–H interlayer and gel pores. c) The interlayer–4 nm and 1–4 nm connected pore model. The (100) surface composition is shown in the zoomed out figure consisting of water molecules, calcium and non-bridging oxygen atoms. d) The model for the disk–like globule building block highlighting the size from the top and side views of the particle. Color legend: O, red; H, white; Ca, green; Si, yellow.

2.1.3. Disk–like globule model

Subsequently, a globule was modeled following findings from a Small-Angle Neutron Scattering (SANS) experiment [9] which have reported the existence of disk–like C–S–H building blocks (see Figure 1 d)). The radius of the disk is 4.5 nm and the height is 4.4 nm, in agreement with the typical size of the globules reported in CM-II model (*i.e* 4.2 nm across [8]). The disk–like globule model exposes the edge surfaces composed of mainly deprotonated oxygen and calcium atoms. Additional O sites are protonated to ensure charge neutrality

of the globule particle. The disk–like C–S–H particle constituted by 26946 atoms was then immersed in an 11.5×11.5×7.5 nm^3 simulation box with 22784 water molecules. With this box size, the shortest distance between two adjacent globule particles is ≈ 2.5 nm perpendicularly and 3.0 nm radially.

2.2. Computational details

The molecular dynamics simulations were performed using LAMMPS [43] simulation package. The interatomic interactions of C-S-H are described using the modified CLAYFF force field [44–46]. The flexible version of the SPC model by Teleman et al. [47] is used in the description of the water molecules. Each simulation consisted of an initial equilibration of 2 ns in NPT ensemble and an additional 5 ns in NVT ensemble to generate trajectories for post-processing. A longer production run of 20 ns was performed to analyze exchange in connected pores. The time step, temperature, and pressure conditions are 0.5 fs, 300 K, and 1 atm respectively. Periodic boundary conditions are applied in all three dimensions. The Coulomb interactions are modeled using the PPPM [48] method with a precision of 10^{-5} and a cutoff of 10 Å for pair interactions.

The short time water dynamics behavior (*i.e* femtosecond scale) is investigated by performing vibrational dynamics calculations. The analysis is based on the vibrational density of states (VDOS) calculated from the Fourier transform of the atomic velocity autocorrelation function (Equation 1) of the water's oxygen and hydrogen atoms velocity trajectories.

$$VDOS = \int_0^t \frac{\langle v(t_0) \cdot v(t) \rangle}{\langle v(t_0)^2 \rangle} cos(\omega t) dt \tag{1}$$

where $v(t_0)$ and $v(t)$ are the velocities of a certain atom at an initial time t_0 and a certain later time t respectively. The angular brackets denote the averaging over both the number of atoms N and time origins N_T. The velocity snapshots were saved every timestep (0.5 fs) for 100 ps. Since the period of the water vibrations is much less than 1 ps [49], the length of the trajectory was deemed satisfactory for the analysis.

Translational dynamics of the confined water are studied by calculating the self–diffusion coefficient, D. D is calculated based on the Einstein's relation [50], *i.e*

$$D = \lim_{t\to\infty} \frac{\langle [\mathbf{r}_i(t) - \mathbf{r}_i(0)]^2 \rangle}{2dt} \tag{2}$$

where $\mathbf{r}_i(0)$ and $\mathbf{r}_i(t)$ are the position vectors at the initial and a later time t, respectively. The angled brackets indicate an ensemble average and d the dimensionality. Equation 2 is modified in the calculation of parallel diffusion ($D_{||}$) within slabs to take into consideration the survival probability function, as described in details in ref. [51].

The reorientation of the water molecules is accounted for by the HH intramolecular vector autocorrelation function, $C_{HH}(t)$ (Equation 3). The rotational correlation time, τ_c is calculated by fitting $C_{HH}(t)$ (Equation 3) to a stretched exponential function $a_0 e^{-(t/\tau_c)^\beta}$. A stretched exponential function with $0 < \beta < 1$ has been shown to describe well the long-time relaxation behavior of autocorrelation functions of supercooled and confined water[52, 53].

$$C_{HH}(t) \quad = \quad \frac{1}{2}\langle 3\cos^2\theta(t) - 1\rangle \tag{3}$$

$\theta(t)$ denotes the angle formed by the HH unit vectors at time t.

The calculation of the T_2 relaxation time follows the semiclassical theoretical description of spin relaxation by Bloembergen, Purcel and Pound (BPP Theory) [54]. According to BPP theory, the T_1 and T_2 relaxations of proton bearing fluids are facilitated by dynamic fluctuations in the local magnetic fields, arising from intra- and inter- nuclear magnetic dipole-dipole interactions. The corresponding autocorrelation function, $G_{R,T}(t)$, of the fluctuating magnetic dipole-dipole interactions is given by;

$$G_{R,T}(t) = \frac{3}{16}\left(\frac{\mu_0}{4\pi}\right)^2 \hbar^2\gamma^4 \frac{1}{N}\sum_{i\neq j}^{N} \left\langle \frac{3(cos^2\theta_{ij}(t+\tau) - 1)}{r_{ij}^3(t+\tau)} \frac{3(cos^2\theta_{ij}(\tau) - 1)}{r_{ij}^3(\tau)} \right\rangle_\tau \tag{4}$$

where μ_0 is the permeability of free space, $\hbar$ is the reduced Planck's constant, γ is the gyromagnetic ratio, t is the lag time in the autocorrelation, r_{ij} and

θ_{ij} are the distance and angle between spins i and j respectively, and N is the number of interacting spins of spin I = 1/2. The subscripts R and T denote the intramolecular and intermolecular spin interactions respectively.

The calculation of T_2 relaxation time, therefore, involved the computation of $G_{R,T}(t)$ from the hydrogen atom position trajectories, by analyzing the evolution of the relative distances r_{ij} and angles θ_{ij} between the hydrogen atoms of the molecules involved. Once the autocorrelation function $G_{R,T}(t)$ is determined, $T_{2,R,T}$ is calculated from the following equation:

$$\frac{1}{T_{2,R,T}} = \frac{3}{2}J_{R,T}(0) + \frac{5}{2}J_{R,T}(\omega_0) + J_{R,T}(2\omega_0) \tag{5}$$

where $\omega_0 = \gamma B_0$ is the Larmor frequency and $J_{R,T}(\omega)$ is the spectral density of the local magnetic-field fluctuations determined by the Fourier transform of $G_{R,T}(t)$:

$$J_{R,T}(\omega) = 2\int_0^\infty G_{R,T}(t)cos(\omega t)dt \tag{6}$$

In this work, a fast exchange limit is assumed, *i.e* on the timescale of the experiment, the adsorbed molecules are in rapid exchange with those within the pore and diffusion ensures that all molecules experience both environments equally [55]. The total T_2 relaxation for the water molecules within the pores is thus a summation of both the surface and bulk relaxations. This assumption implies that $\omega_0\tau_{R,T} << 1$ and $J(0) = J(\omega_0) = J(2\omega_0)$. Therefore;

$$\frac{1}{T_{2,R,T}} = 5J_{R,T}(0) \tag{7}$$

The exchange time for an interlayer–4 nm and 1–4 nm connected pores was analyzed by fitting the survival probability function $P(t)$ to a biexponential function: $A_1e^{t/\tau_1} + A_2e^{t/\tau_2}$.

$$P(t) = \langle N(t)/N(0)\rangle \tag{8}$$

where $N(t)$ and $N(0)$ are the number of water molecules at time t and $t = 0$ respectively. Only the water molecules which remain in the specified pore during

the entire simulation time were considered in the survival probability function calculation. Two exchange times, τ_1 and τ_2 are obtained after fitting the survival probability function $P(t)$ (Equation 8) to a biexponential function, where, the larger value is associated with the slow desorption rate and vice versa.

3. Results and Discussion

3.1. Infinite planar pores

3.1.1. Atomic density profiles

The atomic density profile of the water oxygen (O_w), water hydrogen (H_w), silicate silicon (Si) and silicate oxygen (O) atoms along the z direction is shown in Figure 2 a). The O_w density profile in all the gel pores is characterized by a shoulder at $z \approx 1.0$ Å and a peak at $z \approx 2.5$ Å from the surface (see Figure 2 a) for a 2 nm pore). The shoulder is attributed to the water molecules trapped within the channels formed by the silicate chains running along the [010] crystallographic direction, while the peak is formed by the water molecules at the surface interface (Figure 2 b)). Due to their location, these water molecules are expected to form hydrogen bonds with the surface non–bridging O atoms. The H_w density profile in both the interlayer and gel pores (Figure 2 a)) further demonstrates that water hydrogen atoms are pointing towards the C–S–H model substrate: an indicator of the hydrophilicity of C–S–H [56].

The structuring of water near the C–S–H model surface is viewed as weak due to the formation of less sharp peaks for the O_w and H_w density profiles (Figure 2 a)). This is attributed to the broken silicate chains which disturbs the local surface structure resulting in a weaker layered packing of the surface water molecules. This feature is expected for defected tobermorite models [23–25], in contrast to the sharply defined maxima of the density profile within a narrow range of values characteristic of hydrophilic surfaces [57–59] and tobermorite crystal analogs [60]. The bulk water density (0.033 molecules/Å^3) is attained at ≈ 7 Å from the surface.

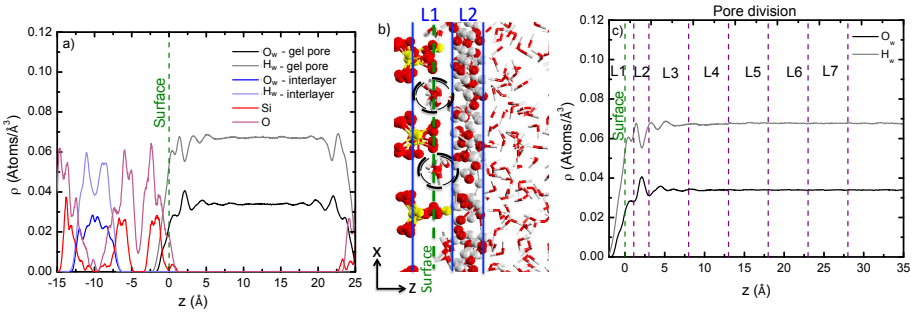

Figure 2: a) The atomic density profile of the oxygen (O_w) and hydrogen (H_w) atoms for the interlayer and gel pore water molecules, the silicate silicon (Si) and oxygen (O) atoms. b) The C–S–H model surface details highlighting the location of water within the silicate channels (L1) and the interface water in L2 region. Color legend: O, red; Si, yellow; H, white. The surface is defined as the average position of the non–bridging oxygen atoms. c) Gel pore subdivisions based on the O_w density profile.

Although the gel pore water density profile is bulk–like after just a few Å from the surface, studies have shown that the corresponding water dynamical properties are perturbed for larger distances in nanoconfined geometries [58]. To analyze the role of the surface on the dynamical properties of water in C–S–H, the pores were subdivided into 7 slabs (see Figure 2 c)). L1 and L2 slabs were categorized as the subsurface and interface water molecules respectively, following the boundaries of the density profile. In relation to the CM-II model, the surface adsorbed water (modeled here by L1 and L2 water molecules) can be understood as water present in empty gel and capillary pores [8]. However, for filled pores (as in our case), these water molecules are reclassified as gel pore water as noted experimentally in NMR measurements of the water content of different pore types [61]. Beyond L2, the slabs namely L3, L4, L5, L6 and L7 (see Figure 2 c)) are each of 5 Å, making our analysis up to 28 Å from the defected tobermorite surface. This choice makes sure the properties of water in the middle of each pore are studied.

3.1.2. Vibrational Dynamics

The discussion of the vibrational dynamics is focused on making a connection between the experimental infrared/Raman/INS spectra of bulk water within the frequency range of 0 to 4000 cm^{-1} and the VDOS obtained from our MD results. In this frequency range, the contribution to the VDOS of bulk water emanates from intermolecular and intramolecular motions. The intermolecular motions contain information about the translational (10–400 cm^{-1}) and librational/rotational (400-1200 cm^{-1}) motions. Beyond 1200 cm^{-1}, the contribution to the VDOS comes from the intramolecular motions [62, 63].

As shown in Figure 3 a) for an oxygen atom spectra, the O$\cdots$O$\cdots$O bending mode of triply hydrogen bonded water molecules for the 2–5 nm pores is located at $\approx$ 50 cm^{-1} and it coincides with the bulk water peak. This intersection indicates that increasing the pore sizes facilitates the formation of a 3D network with bulk–like vibrations for pores as small as 2 nm. In contrast, there is a significant shift to 60 cm^{-1} and 80 cm^{-1} for the 1 nm and interlayer pore respectively. The blue shift (to higher frequencies) for small pores is understood as an indicator of reduced translational degrees of freedom [62, 63]. Within this frequency range, the inelastic neutron scattering (INS) spectrum for hydrated cement displays a low frequency peak at $\approx$ 80 cm^{-1} [17], which based on our findings, can be correlated to water confined in pores of sizes $<$ 1 nm. Blue shifting of the O$\cdots$O$\cdots$O bending mode has also been observed in other confined geometries [62], supercooled water [64, 65] and bulk water at high pressures [66].

The intermolecular O$\cdots$O stretching modes appearing between 200–300 cm^{-1} are very weak, and we observe no appreciable difference between bulk water and the gel pores (Figure 3 a)). The red shift of the O$\cdots$O stretching modes, linked to the formation of a 2D hydrogen bond network in extreme confinement [63], is only evident for water nanoconfined in interlayer pore spaces.

The hydrogen atom VDOS is shown in Figures 3 b)–d). We observe a shifting of the translational peak centered around 48 cm^{-1} with increasing confinement (Figure 3 b)), which we associate with reduced translational dynamics. Neutron

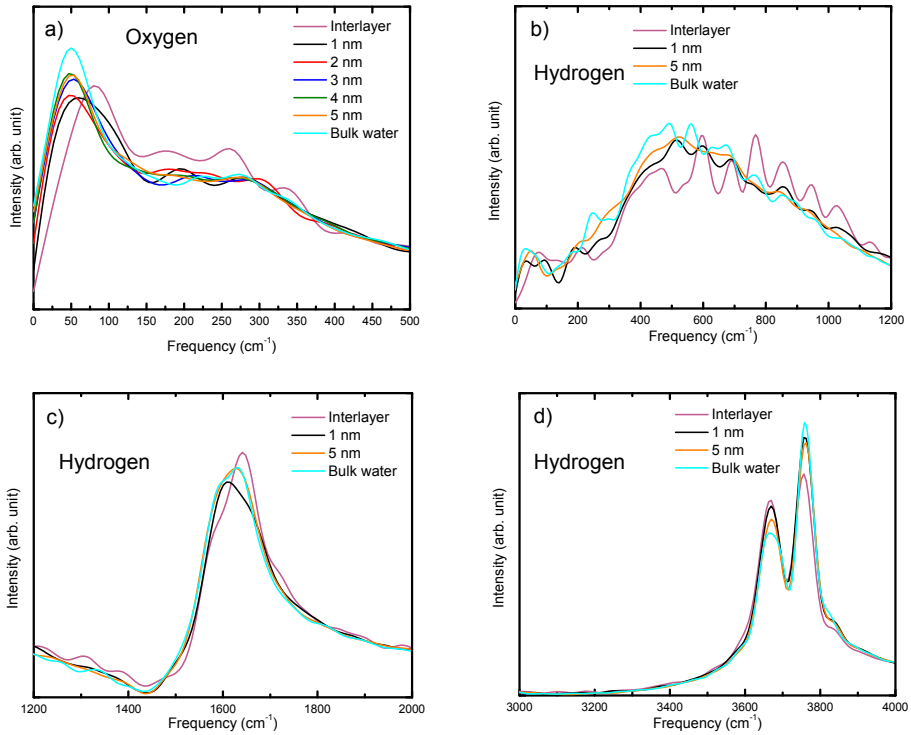

Figure 3: a) Oxygen atom VDOS for the water within the interlayer and gel pores (1–5 nm) of a C–S–H model in comparison to bulk water. Hydrogen atom VDOS for water in the interlayer, 1 nm, 5 nm and bulk in the frequency range b) 0–1200 cm^{-1}, c) 1200–2000 cm^{-1} and d) 3000–4000 cm^{-1}.

scattering experiments have instead shown an attenuation of this peak for the water hydrogen atom spectra [17, 62] with confinement. For the librational motions occurring in the 400–1050 cm^{-1} frequency range, we observe a shift of the librational edge to higher frequencies as the pores sizes are decreased (see Figure 3 b) and the Gaussian fits (Figure S1 a)) in the supporting information). Such a shift, also observed for water confined in Vycor glass [62] and clays [67–69] is correlated to the hindrance of motion because of reduced rotational degrees of freedom [62, 63]. Moreover, the sharp peaks observed here for the water in the interlayer pores is a feature known to occur for highly ordered hydrogen

containing systems [68, 70].

The frequencies appearing at ≈ 1600 cm^{-1} (Figure 3 c)) correspond to the intramolecular bending modes. There is a slight blue shift of this band for the water molecules within the interlayer pores regarding bulk water and gel pores (see Figure 3 c) and the Gaussian fits (Figure S1 b)) in the supporting information). This shows that the ability to alter the hydrogen bond network through O–H bending is significantly restricted in the interlayer pore environment, which can be explained by the high surface to volume ratio and the presence of Ca^{2+} cations. The intermixing of the restricted surface water molecules with those away from the surface displaying bulk–like behavior is ascribed to the non-distorted bending modes for the gel pores.

At higher frequencies, the bands at ≈ 3600 cm^{-1} (Figure 3 d)) correspond to the O–H stretching modes [71]. Our results indicate a strong similarity of the spectra of confined water with that of bulk water in this frequency range (Figure 3 d)). Therefore, the surface and pore size effects cannot be retrieved from our simulations in this frequency range.

3.1.3. Translational Dynamics

The diffusivity of the water contained in the interlayer and gel pores was analyzed by plotting the mean square displacement (MSD) as a function of time (Figures 4 a) and b)). The dynamically slow nature of the water within the interlayer pore spaces is evident (see Figure 4 a)) and follows the relaxing cage model developed for supercooled water [72, 73], where the diffusion can be separated into four stages: ballistic, cage, transition and diffusion regimes. The ballistic regime ($t \leq 200$ fs) is apparent in all the pores and during this period, the water's MSD is proportional to t^2. Next is the cage stage which is characterized by a plateau up to ≈ 1 ps caused by water molecules rattling around a cage created by neighboring water molecules and ions. This plateau, clearly visible in the interlayer pores, fades away as the pore sizes are increased. During the transition stage, the MSD $\propto t^{\beta}$ where $\beta < 1$. Lastly, it is the diffusive regime where the MSD varies linearly with time. During the first 100 ps (Figure 4 a)),

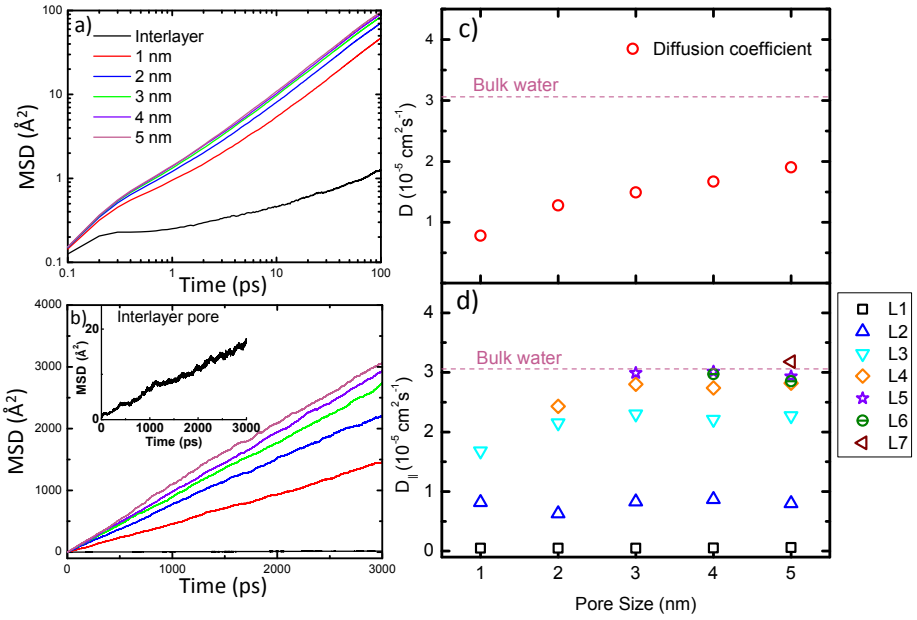

Figure 4: MSD as a function of time during a) the first 100 ps and b) a period of 3 ns for the interlayer and gel pores (1–5 nm) of a C–S–H model. The key of graph b) is the same as shown in a). c) Variation of self–diffusion coefficient (D) of water confined in a C–S–H model with pore size. d) $D_{||}$ as a function of distance from the C–S–H model substrate.

the water in 1–5 nm pores already reaches the diffusive regime while for the interlayer water, the root-mean-square displacement (RMSD) is still < 2 Å; a characteristic of immobile water [56, 74]. Therefore, the classification of water in the interlayer of C–S–H as bound within the QENS experimental timescale [17] can be understood from this analysis.

The dependence of self–diffusion coefficient (D) on pore size (Figure 4 c)) follows the well-known trend of fluids in confined geometries: D increases with increase in pore size [75, 76]. The slowdown factor varies from 1.6–4 as the pore sizes are reduced from 5–1 nm. This implies that within the gel pores, some water molecules behave like bulk, as shown from the diffusional analysis of unbound water in cement [17, 77]. For the interlayer pores, D is 0.02×10^{-5}

cm^2s^{-1}: two orders of magnitude lower than for the bulk water. Other MD simulation works by Bhatt et al. [78] and Li et al. [25] reported 0.009 $\times 10^{-5}$ cm^2s^{-1} and 0.003 $\times 10^{-5}$ cm^2s^{-1} for the D of water within the interlayer of C–S–H models respectively. The slightly dissimilar models (*i.e* D varies with Ca/Si ratio [74]) may explain the variation of the values from different MD simulations. Nevertheless, the hindered translational dynamics of the interlayer water is clear from these analyses. The reduced water self-diffusion has also been observed for water molecules confined in the interlayers of layered double oxide phases [79–81] and clay minerals [82, 83].

The parallel self–diffusion coefficient ($D_{||}$) of the water molecules in L1 (water within the surface silicate channels) in all the pores is $\approx 0.05 \times 10^{-5}$ cm^2s^{-1} (Figure 4 d)). This finding is experimentally confirmed by ^{1}H NMR field cycling relaxation experiments [13] for water in cement paste where the self–diffusion coefficient of the surface water is $\approx 1/60$ that of bulk water. Averaging over all water molecules associated with the surface (L1 and L2 regions), we obtained $D_{||}$ as 0.3×10^{-5} cm^2s^{-1}. Considering that as water reacts with cement the bulk–like component of water eventually disappears, this value corresponds mostly with constrained water *i.e* strongly interacting with the surface and confined mainly in small gel pores and intraglobular water.

Moving away from the surface, the water located beyond L2 (*i.e* 3 Å from the surface) is fast moving with a self–diffusion coefficient of the same order as bulk water (see Figure 4 d)). The fast translational water dynamics in slabs L3 to L7 is attributed to the bulk–like density in this region [58, 59]. Nevertheless, the $D_{||}$ value for water within 1 and 2 nm pores is lower than the bulk water value even in the middle of the pores.

3.1.4. Rotational Dynamics

The dependence of τ_c with pore size is reported in Figure 5 a), where it is shown that τ_c decreases with increasing pore size. For the smallest gel pore (*i.e* 1 nm), τ_c is about five times longer than the bulk water value (1.41 ps) calculated using the same force field. This finding is in quantitative agreement

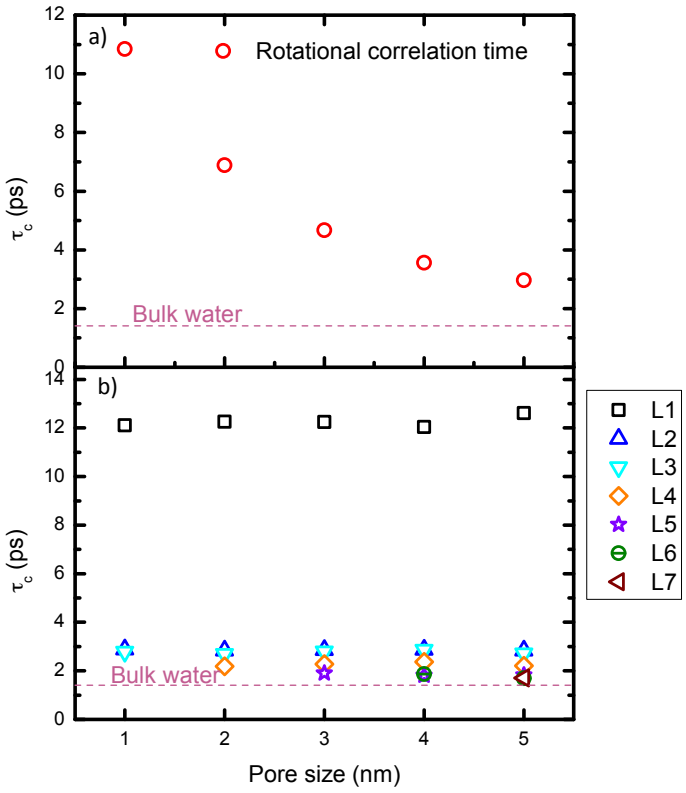

Figure 5: a) Variation of the rotational correlation time, τ_c of water confined in C–S–H model with pore size. b) τ_c as a function of the distance from the C–S–H model substrate.

with the results for hydration water in dicalcium silicate [84]. The restrictions in the rotational degrees of freedom in small pores [85], are seen as a consequence of the rearrangement of the hydrogen bond network in confinement, which has been shown to promote enhancement of the hydrogen bond strength [86]. For the water in interlayer pores, τ_c is 38.52 $\pm$ 1.02 ps, in this case, the decay of $C_{HH}(t)$ is slow (Figure S2 and Table S1 in the supporting information), which further supports the immobile nature of the water within the C–S–H particle. The slowdown in rotational dynamics for water confined in C–S–H is in broad agreement with water confined in other systems [87, 88].

From the local rotational dynamics investigated by the calculation of τ_c in each slab, it is evident from Figure 5 b) that the rotational relaxation is surface-dominated only in L1 region, which we associate to the restricted location of the water molecules within the silicate channels. The corresponding residence time in L1 is 168 ±0.6 ps. Our calculated residence time is relatively shorter than for other hydrophilic surfaces [58]; a suggestion of a lower surface affinity for the C–S–H model surface. This is in agreement with theoretical models [89] for mortar and MD simulations of water confined in tobermorite and silica nanopores [24].

The τ_c values converge to a single value beyond L3 (Figure 5 b)). This implies that the stabilization of the hydrogen bond network by the C–S–H pore surfaces is short ranged, beyond which the local rotational dynamics are independent of the surface. There is notably fast reorientational dynamics in L2 slab, which, despite the water molecules forming hydrogen bonds with the surface non–bridging oxygen atoms, is of the same order as water in the pore centers. This can be explained by the weak adsorption in L2, evidenced by the short residence time of 3.75 ±0.4 ps. This differs from the translational dynamics, where we have shown in the previous section that $D_{||}$ in L2 is one order of magnitude slower than bulk water. This finding highlights the decoupling of the translational and rotational water dynamics within C–S–H nanopores.

Our results suggest that the surface water rotation rate is linked to the rate of desorption. Since reorientation occurs in parallel with the breaking and forming of H-bonds, it can be inferred from our calculations that the reorientation mechanism involves large–amplitude jumps as described extensively by Laage et al. [90, 91].

3.1.5. NMR T_2 Spin Relaxation

The dominant ^{1}H NMR relaxation mechanism in cement involves the interaction of magnetic dipolar with surface paramagnetic impurities. The characteristic relaxation times may vary depending on the composition, age, and the hydration/drying conditions [92]. Bearing in mind that our cement model

lacks paramagnetic ions, our discussion is within the context of understanding possible contributors to relaxation rate dispersions (independent rotational and translational contributions), which emanates from the slow-moving proton spins contained within the surface layer and in the bulk–like region.

The variation of the correlation functions $G_R(t)$ and $G_T(t)$ (Equation 4) due to rotational and translational dynamics respectively on the surface (L1 and L2), bulk–like regions (beyond L2) and within the interlayer pores is shown in Figure 6. The decay of the translational component ($G_T(t)$) is faster than the rotational counterpart for the interlayer and surface water. This is an implication that the surface relaxation in C–S–H model pores is dominated by the translational motions, in agreement with water confined in calcite slit pores [58]. Hence, this justifies the neglection of the rotational dynamics for spin relaxation models dominated by surface relaxation [14, 24, 93]. The rotational hindrance on the surface and the interlayer pore spaces may be due to steric effects caused by the surface atoms and the Ca^{2+} ions.

Within the bulk–like region, a more rapid drop of both translational and rotational components is evident, which we attribute to the fast dynamics in this region. However, in contrast to the surface region and interlayer pores, the rotational component $G_R(t)$, decays faster in the bulk–like region. The increased noise in the gel pore rotational component is due to a possible jump reorientation mechanisms [90] and poor statistics since there are fewer intramolecular spin pairs than intermolecular spin pairs.

The calculated T_2 relaxation times for water on the surface and in the bulk–like region are shown in Figure 7 a). In the surface region, the T_2 relaxation times are one order of magnitude lower than in the bulk–like region and pore size independent. The differing T_2 relaxation times in these two regions are as a consequence of the slow-moving proton spins contained in the surface layer in comparison to the bulk–like region. Since the contribution emanating from the interaction of electronic spins with paramagnetic ion impurities in the confining pore matrix is not considered, the short surface region T_2 relaxation time highlights the role played solely by the translational and rotational dynamics in the

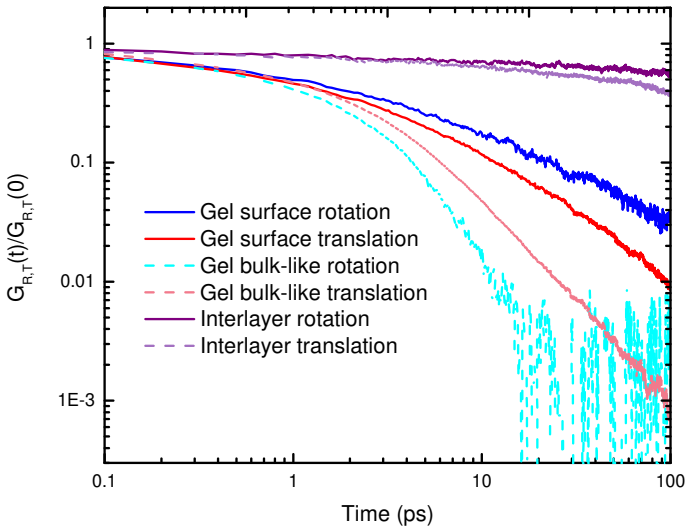

Figure 6: Normalized translational and rotational dipolar correlation function, $G_{R,T}(t)/G_{R,T}(0)$ for an interlayer pore, surface and bulk–like water molecules.

modulation of the dipolar spin-spin interaction. These results are in qualitative agreement with experimental observations that surface interactions help lower the relaxation time [14, 78, 93].

The total T_2 relaxation time of water within C–S–H pore model averaged over the surface and bulk relaxation according to the fast exchange model [94] is shown in Figure 7 b). The trend of the NMR T_2 relaxation time reflects the general sensitivity of NMR measurements to pore-size distributions, where a lower T_2 is expected for small pores, whereas, large pores result in higher T_2 relaxation time values. For mature cement, four T_2 components are identified which correspond to the solid hydrates (*e.g* portlandite ($Ca(OH)_2$)), interlayer water, gel pore water and water in capillary pores. The assignment of the T_2 relaxation time values is 10 μ s, 100 μ s, 340 μs and $>$ 1 ms respectively [92, 95–98]. Within the interlayer pores, the calculated T_2 relaxation time is 0.15 s; $\approx$ 3.6 times smaller than for the smallest gel pore (*i.e* 1 nm pore). The slowdown factor between interlayer and gel pores obtained here is remarkably similar to the 3.4 value from experiments [92, 95–98]. Considering that the ratio of T_1/T_2

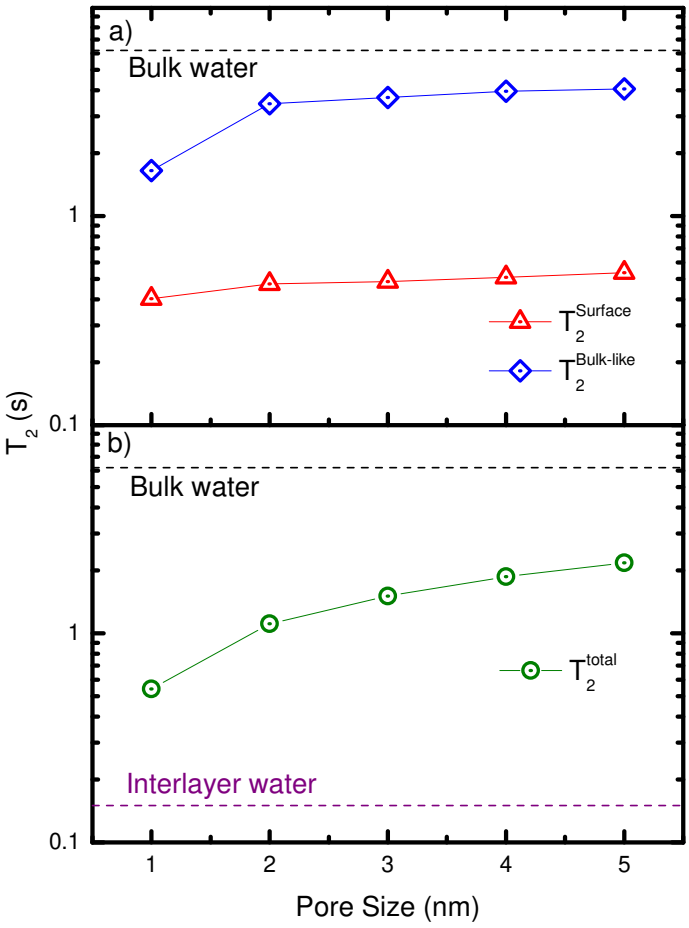

Figure 7: a) T_2 relaxation time of the water associated with the surface and bulk–like regions of the C–S–H model pores. b) The overall T_2 relaxation time of water averaged over the surface and bulk regions contributed by the translational and rotational dynamics. The y-axis scale is logarithmic.

is ≈ 4 in cement paste [99, 100], our calculations are in good agreement with MD calculations by Bhatt et al. [78] for an interlayer and a 1 nm C–S–H model pore where they reported T_1 relaxation time values of 1.47 s and 2.75 s respectively using a similar approach.

3.2. Interpore Exchange of Water in C–S–H

3.2.1. Exchange Rate

There was no appreciable desorption from the interlayer pores during the entire simulation time (Figure S3 in the supporting information). Based on our C–S–H atomistic model, a possible explanation for the lack of water desorption from the interlayer pores is due to the presence of Ca^{2+} ions and broken silicate chains which facilitate enhanced hydrophilicity of the C–S–H coupled with the extremely restricted pore space. In real cement paste, more complex pore system is expected to play a big role.

A fitting was thus done only for the 1–4 nm connected gel pores. The resultant τ_1 and τ_2 values after fitting the survival probability function $P(t)$ (Eqn. 8) to a biexponential function are 2.68 ns and 18.94 ns respectively. This suggests that there is exchange of water between a 1 and 4 nm connected gel pores, albeit faster than the value reported experimentally [27]. τ_2 is taken as the exchange time between a 1 and 4 nm connected pore while the fast desorption time, τ_1 is interpreted as possibly due to the water molecules on the pore boundaries.

3.2.2. 2D T_2–T_2 NMR Relaxation

Since there is no significant exchange between our interlayer and the 4 nm model pores, T_2–T_2 NMR relaxation analysis was done for only the 1–4 nm connected pores. The initial T_2 relaxation time was calculated for each pore separately by averaging over all water molecules remaining within the pore within a simulation time of 5 ns. This approach implies that the fast exchange limit in our calculation is assumed only between the surface and the bulk–like water. This is justified because the calculated surface residence time is much shorter than exchange time between the pores (*i.e* 168 ps compared to 18 ns; 2 orders of magnitude). Thus, at the initial time, we have only two values of T_2 relaxation time (see Figure 8). Subsequent calculations of T_2 were performed after successive delay times (τ_{delay}); 1 ns, 2 ns, 3 ns, 4 ns and 5 ns.

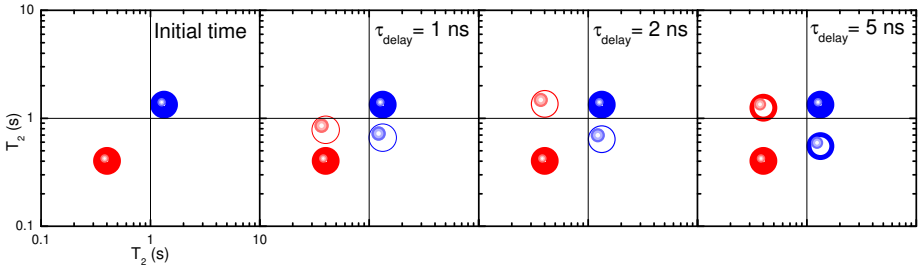

Figure 8: T_2–T_2 relaxation time between a 1 and 4 nm connected gel pores at an initial time and subsequent delay times (1 ns, 2 ns and 5 ns). The filled spheres denote the calculated T_2 relaxation time for water molecules within the 1 nm (red) and 4 nm (blue) pores at the initial time. On the other hand, the empty spheres denote the calculated T_2 relaxation time for the water molecules that have moved from 1 nm to 4 nm (red) and 4 nm to 1 nm (blue) pores after a certain delay time. The increasing thickness of the empty spheres indicate the relative increase of the number of exchanged water molecules after longer delay times.

At the initial time, the calculated T_2 relaxation time for the 1 nm and 4 nm pores is 0.4 and 1.4 s respectively. The slightly lower value for the 4 nm pore in comparison to the slit pores (1.8 s) could be due to confinement along the (100) direction, rather than the (001) for the infinite slit pores. After a certain delay time τ_{delay}, some molecules exchange between the pores, and thus their T_2 relaxation time is expected to correspond to the new pore environment [27, 34, 101]. Considering that we know the pore sizes, here, the T_2 relaxation time is calculated for only the water molecules which have moved to a different pore during the delay time. This approach enables progressive monitoring of the relaxation dynamics of the water molecules with time, hence, a possible indicator of the local environment.

After a 1 ns delay, the T_2 relaxation time for the water molecules which moved from the 4 nm to the 1 nm pore is 0.66 s while those from 1 nm to 4 nm is 0.78 s. These values are very similar, and are different from T_2 relaxation times of the corresponding pores. This is an implication that after 1 ns, although

some water molecules exchange, they are still trapped in the pore entries and/or edge surfaces, where the relaxation may be faster for a 1 nm pore and slower for a 4 nm pore.

Subsequent calculations after 2, 3, 4 and 5 ns show that the water moving to the 4 nm pore attains the average pore T_2 relaxation time (see Figure 8 after 2 and 5 ns delay times). Our results indicate that the exchange of water within the connected pore model is not similar in both directions. After 2 ns, the water molecules entering the 4 nm pore register the same T_2 relaxation time as the entire pore. In contrast, the T_2 relaxation time for water entering the 1 nm pore does not reach the value obtained at the initial time. It can be concluded therefore that, within our simulation time, the entry of water into the 1 nm gel pores is limited only to the edges, where the T_2 relaxation time and other dynamical properties *e.g* self–diffusion and rotations might be different from those at the center of the pores. This desorption behavior, also reported by Feldman et al. [102, 103] based on water sorption experiments of cement paste, has been associated with the hysteresis in the variation of Young's modulus, flexural strength, length, and weight change with relative humidity.

3.3. The Particulate Nature of C–S–H

The discussion in this section is limited to a quantitative comparison of the translational and rotational dynamics of water on the surfaces of a disk–like C–S–H globule particle and water within the infinite interlayer and gel pores (section 3.1). Near a disk–like globule, the two pore environments explored include: inner ($R < 2.0$ nm) and outer ($R > 4.5$ nm) regions from the center of the disk particle termed as C1 and C2 regions respectively (see the illustration of the two regions in Figures 9). Within C1, the calculations were done on slabs along the z direction which implies that we analyze water in a confinement environment of two finite planar disks, while in C2, the water dynamics in slabs radially around the disk are studied.

As shown in Figure 9 a), in region C1, $D_{||}$ is low within the interlayer pore spaces and approximately two hydration layers from the C–S–H globule surface.

In the middle of two adjacent C–S–H globules stacked along z direction, the $D_{||}$ values are lower than for bulk water, which is attributable to confinement effects and desorbed Ca^{2+} ions. In the C2 region which represents the edge surfaces, the diffusion of water molecules is slow and does not demonstrate any confinement effects within a 5 Å radius (slab 1) from the surface, since x, y and z D components are equal (Figure 9 b)). Moving away from the edge surface, confinement effects are seen in the x and y directions.

Quantitatively, it was noted that the self–diffusion coefficient values on the planar disk–top surface (which is the same surface as for the infinite planar gel pores; Figure 9 a)) and radially (edge–edge surface; Figure 9 b)) are similar to those obtained for the water in L1 region of the infinite gel pores (*i.e* order of 10^{-7} cm^2s^{-1}). Since the radial slabs are larger than for the planar surface (*i.e* 5 Å as opposed to 3 Å), we can infer from our calculations that the translational dynamics are more restricted on the edge–edge surfaces in comparison to the basal surfaces. The slow dynamics are attributed to water molecules which are interacting with the complex edge surfaces constituted by Ca^{2+} ions and broken silicate chains. These findings, which are in agreement with NMR experiments [13] for water diffusion on cement surfaces, emphasize the role of pore surface chemistry on water diffusion properties.

The rotational dynamics are evidently slow on the C–S–H globule surface and interlayer pores (see Figure 9 c) and d)). Although within the interlayer space of the globule, water exhibits similar rotational dynamics as for infinite planar pores, τ_c is slightly longer on the surfaces of the C–S–H globule than in infinite planar pores. Additionally, on the edge–edge surface, we observe a more gradual decrease of τ_c, suggesting a more stable hydrogen bond network in this environment (Figure 9 d)). Nevertheless, our results indicate that the C–S–H globule surface impacts water dynamics in an analogous way as infinite planar pores, giving rise to faster rotational dynamics in relation to translational dynamics—implying translational–rotational decoupling.

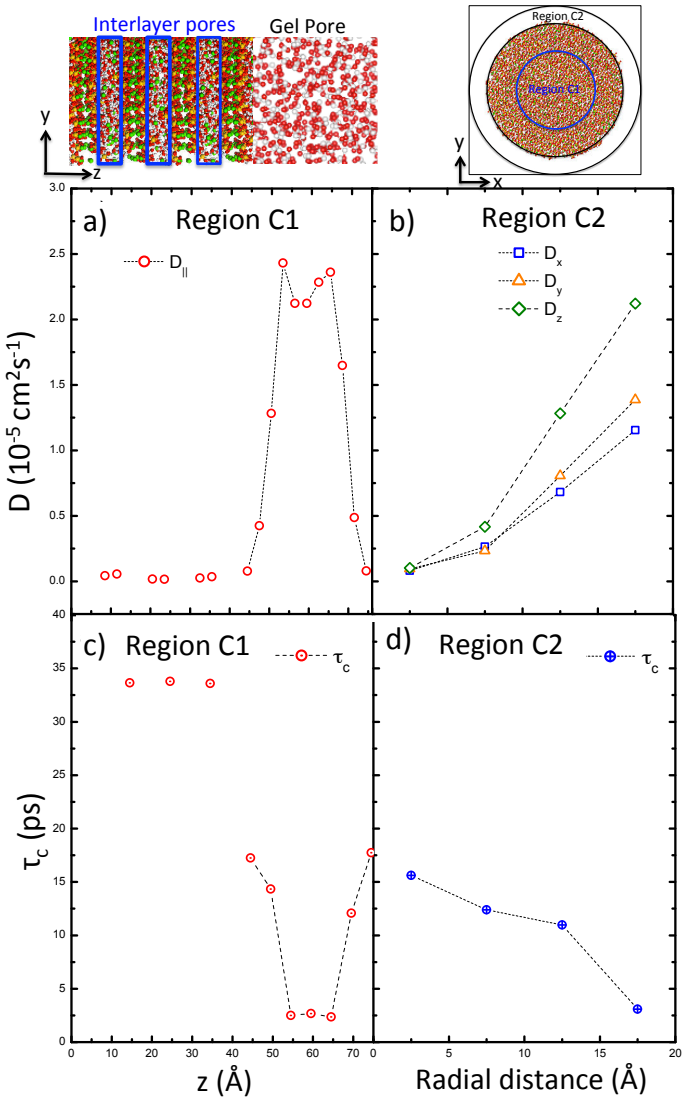

Figure 9: a) 2D self–diffusion coefficient $D_{||}$, of water in a disk–like C–S–H model particle in slabs along the z direction (Region C1). b) 1D self–diffusion coefficient along the x, y and z directions in radial cross section slabs (Region C2). c) Rotational correlation time τ_c, of water confined in disk–like C–S–H model particle in slabs along the z direction (Region C1). d) τ_c in radial cross section slabs (Region C2).

4. Conclusions

Extensive dynamical properties of water within the interlayer and gel pores of C–S–H were investigated via atomistic simulations. The four pore environments considered include infinite planar interlayer and gel pores, connected pores and finite pore space created by arrangement of disk–like globule particles. From our analysis, the dynamics of water within C–S–H can be separated into two: slow dynamics associated with the surface and interlayer water molecules and fast dynamics characteristic of the middle of the gel pores of sizes as small as 2 nm.

The effect of the C–S–H surface chemistry was investigated using infinite planar models and C–S–H globule particles. The overall slow surface water dynamics are associated with the specific geometry of the silicate chains and the presence of Ca^{2+} ions on the surface. In both the infinite planar and edge surfaces of the finite globule, we observed translational–rotational decoupling where the rotational dynamics are faster than translational dynamics. The relatively faster rotational dynamics and the short surface residence times which are linked to hydrogen bond making and breaking suggest a weak surface affinity of the C–S–H model surfaces. The C–S–H surface affinity is expected to differ in high Ca/Si ratio C-S-H models due to the presence of more surface Ca^{2+} ions in addition to the broken silicate chains which collectively enhance cohesion in C–S–H.

Overall, there is a slowdown of the water dynamics as the pore sizes are decreased from 5 to 1 nm. We observed a significant blue/red shift of the vibrational modes only in very small pores (interlayer and 1 nm). For all the properties studied, the immobile nature of the interlayer water was clear, which explains the neutron experiment's classification of intraglobular water in C–S–H as bound water. Hence, although the interlayer water is known to influence creep and shrinkage [8] processes, the very slow water motion in these pores is not expected to significantly promote fluid transport related detrimental processes such as chloride-induced corrosion and sulfate attack in concrete structures.

Analysis of the exchange between C–S–H connected pores reveals that within the time limit of our molecular dynamics simulations, there is hardly any desorption from the interlayer pores. Based on our C–S–H pore model, the lack of desorption from interlayer pores is explained by their small size as well as the presence of Ca^{2+} ions which further hinder water mobility. The restricted desorption of water in the interlayer space is associated with reversible shrinkage and creep processes in concrete [104]. Notably, our T_2–T_2 analysis revealed that at short times, the adsorption, or desorption of water from a 1 nm pore may be limited to the edges. The desorption behavior of the 1 nm pore inferred from our studies has previously been linked to the hysteresis in the variation of Young's modulus, flexural strength, length, and weight change with relative humidity [102, 103].

We did not observe any remarkable difference between water dynamics on the globule particle surfaces and the infinite planar gel pores. This result which highlights the importance of the C–S–H surface chemistry in driving the properties of water in its proximity also validates the infinite planar pore models used extensively in atomistic simulations. Additionally, comparison between the edge–edge surface confinement environment and the top planar surface only yielded slight variations.

These findings highlight the state of water within different pore environments of C-S-H, based on the water dynamical properties. Explicit treatment of all the features explored could help improve the analysis of fluid transport, cohesion, and mechanics of cement. Bridging the gap between the results obtained for water within the pore geometries studied in this work and the complex pore network of C-S-H requires the development of a bottom-up multiscale modeling framework. We have shown that it is possible to build and simulate stable C–S–H globule particles of similar shape and size as observed experimentally. As a first step towards upscaling, future work can focus on studying the behavior of water confined in an assembly of few globules.

Acknowledgements

The authors acknowledge the financial support from CAPES, CNPq and São Paulo Research Foundation (FAPESP) Grant No. 17/02317-2. The simulations were performed using USP and USP–RICE Bluegene computational facilities.
Competing Interests: The authors declare no conflict of interest.

References

[1] H. F. Taylor, Cement chemistry, Thomas Telford, 1997.

[2] M. B. Pinson, E. Masoero, P. A. Bonnaud, H. Manzano, Q. Ji, S. Yip, J. J. Thomas, M. Z. Bazant, K. J. Van Vliet, H. M. Jennings, Hysteresis from multiscale porosity: Modeling water sorption and shrinkage in cement paste, Physical Review Applied 3 (6) (2015) 064009.

[3] H. M. Jennings, Colloid model of c- s- h and implications to the problem of creep and shrinkage, Materials and Structures 37 (1) (2004) 59–70.

[4] H. M. Jennings, E. Masoero, M. B. Pinson, E. G. Strekalova, P. A. Bonnaud, H. Manzano, Q. Ji, J. J. Thomas, R. J.-M. Pellenq, F.-J. Ulm, et al., Water isotherms, shrinkage and creep of cement paste: hypotheses, models and experiments, in: Mechanics and Physics of Creep, Shrinkage, and Durability of Concrete: A Tribute to Zdeňk P. Bažant, 2013, pp. 134–141.

[5] T. C. Powers, T. L. Brownyard, Studies of the physical properties of hardened portland cement paste, in: Journal Proceedings, Vol. 43, 1946, pp. 101–132.

[6] R. Feldman, Application of the helium inflow technique for measuring surface area and hydraulic radius of hydrated portland cement, Cement and Concrete Research 10 (5) (1980) 657–664.

[7] H. M. Jennings, A model for the microstructure of calcium silicate hydrate in cement paste, Cement and concrete research 30 (1) (2000) 101–116.

[8] H. M. Jennings, Refinements to colloid model of csh in cement: Cm-ii, Cement and Concrete Research 38 (3) (2008) 275–289.

[9] W.-S. Chiang, E. Fratini, P. Baglioni, D. Liu, S.-H. Chen, Microstructure determination of calcium-silicate-hydrate globules by small-angle neutron scattering, The Journal of Physical Chemistry C 116 (8) (2012) 5055–5061.

[10] L. Skinner, S. Chae, C. Benmore, H. Wenk, P. Monteiro, Nanostructure of calcium silicate hydrates in cements, Physical review letters 104 (19) (2010) 195502.

[11] P. Bonnaud, Q. Ji, B. Coasne, R.-M. Pellenq, K. Van Vliet, Thermodynamics of water confined in porous calcium-silicate-hydrates, Langmuir 28 (31) (2012) 11422–11432.

[12] H. Manzano, E. Duque-Redondo, E. Masoero, I. López-Arbeloa, The role of water on csh gel shear strength studied by molecular dynamics simulations, in: CONCREEP 10, 2015, pp. 899–907.

[13] J.-P. Korb, P. McDonald, L. Monteilhet, A. Kalinichev, R. Kirkpatrick, Comparison of proton field-cycling relaxometry and molecular dynamics simulations for proton–water surface dynamics in cement-based materials, Cement and Concrete Research 37 (3) (2007) 348–350.

[14] J.-P. Korb, L. Monteilhet, P. McDonald, J. Mitchell, Microstructure and texture of hydrated cement-based materials: A proton field cycling relaxometry approach, Cement and Concrete Research 37 (3) (2007) 295–302.

[15] P. J. McDonald, V. Rodin, A. Valori, Characterisation of intra-and inter-c–s–h gel pore water in white cement based on an analysis of nmr signal amplitudes as a function of water content, Cement and Concrete Research 40 (12) (2010) 1656–1663.

[16] E. Fratini, A. Faraone, F. Ridi, S.-H. Chen, P. Baglioni, Hydration water dynamics in tricalcium silicate pastes by time-resolved incoherent elastic

neutron scattering, The Journal of Physical Chemistry C 117 (14) (2013) 7358–7364.

[17] H. N. Bordallo, L. P. Aldridge, A. Desmedt, Water dynamics in hardened ordinary portland cement paste or concrete: from quasielastic neutron scattering, The Journal of Physical Chemistry B 110 (36) (2006) 17966–17976.

[18] F. Ridi, P. Luciani, E. Fratini, P. Baglioni, Water confined in cement pastes as a probe of cement microstructure evolution, The Journal of Physical Chemistry B 113 (10) (2009) 3080–3087.

[19] S. Cerveny, S. Arrese-Igor, J. S. Dolado, J. J. Gaitero, A. Alegría, J. Colmenero, Effect of hydration on the dielectric properties of csh gel, The Journal of chemical physics 134 (3) (2011) 034509.

[20] J. J. Thomas, S. A. FitzGerald, D. A. Neumann, R. A. Livingston, State of water in hydrating tricalcium silicate and portland cement pastes as measured by quasi-elastic neutron scattering, Journal of the American Ceramic Society 84 (8) (2001) 1811–1816.

[21] V. K. Peterson, D. A. Neumann, R. A. Livingston, Hydration of tricalcium and dicalcium silicate mixtures studied using quasielastic neutron scattering, The Journal of Physical Chemistry B 109 (30) (2005) 14449–14453.

[22] P. S. Wang, M. Ferguson, G. Eng, D. Bentz, C. Ferraris, J. Clifton, 1h nuclear magnetic resonance characterization of portland cement: molecular diffusion of water studied by spin relaxation and relaxation time-weighted imaging, Journal of materials science 33 (12) (1998) 3065–3071.

[23] D. Hou, Z. Li, T. Zhao, P. Zhang, Water transport in the nano-pore of the calcium silicate phase: reactivity, structure and dynamics, Physical Chemistry Chemical Physics 17 (2) (2015) 1411–1423.

[24] D. Faux, S.-H. Cachia, P. McDonald, J. Bhatt, N. Howlett, S. Churakov, Model for the interpretation of nuclear magnetic resonance relaxometry of hydrated porous silicate materials, Physical Review E 91 (3) (2015) 032311.

[25] D. Li, W. Zhao, D. Hou, T. Zhao, Molecular dynamics study on the chemical bound, physical adsorbed and ultra-confined water molecules in the nano-pore of calcium silicate hydrate, Construction and Building Materials 151 (2017) 563–574.

[26] A. G. Kalinichev, J. Wang, R. J. Kirkpatrick, Molecular dynamics modeling of the structure, dynamics and energetics of mineral–water interfaces: Application to cement materials, Cement and Concrete Research 37 (3) (2007) 337–347.

[27] L. Monteilhet, J.-P. Korb, J. Mitchell, P. McDonald, Observation of exchange of micropore water in cement pastes by two-dimensional t2- t2 nuclear magnetic resonance relaxometry, Physical Review E 74 (6) (2006) 061404.

[28] S. Jalilvand, R. Shahsavari, Molecular mechanistic origin of nanoscale contact, friction, and scratch in complex particulate systems, ACS applied materials & interfaces 7 (5) (2015) 3362–3372.

[29] D. Hou, Z. Li, Large-scale simulation of calcium silicate hydrate by molecular dynamics, Advances in Cement Research 27 (5) (2015) 278–288.

[30] S. Masoumi, D. Ebrahimi, H. Valipour, M. J. Abdolhosseini Qomi, Nanolayered attributes of calcium-silicate-hydrate gels, Journal of the American Ceramic Society (2019).

[31] R. Gonzalez-Teresa, J. Dolado, A. Ayuela, J.-C. Gimel, Nanoscale texture development of csh gel: A computational model for nucleation and growth, Applied Physics Letters 103 (23) (2013) 234105.

[32] K. Ioannidou, M. Kanduč, L. Li, D. Frenkel, J. Dobnikar, E. Del Gado, The crucial effect of early-stage gelation on the mechanical properties of cement hydrates, Nature communications 7 (2016) 12106.

[33] K. Ioannidou, K. J. Krakowiak, M. Bauchy, C. G. Hoover, E. Masoero, S. Yip, F.-J. Ulm, P. Levitz, R. J.-M. Pellenq, E. Del Gado, Mesoscale texture of cement hydrates, Proceedings of the National Academy of Sciences 113 (8) (2016) 2029–2034.

[34] J. H. Lee, C. Labadie, C. S. Springer Jr, G. S. Harbison, Two-dimensional inverse laplace transform nmr: altered relaxation times allow detection of exchange correlation, Journal of the American Chemical Society 115 (17) (1993) 7761–7764.

[35] X. Cong, R. J. Kirkpatrick, 29 si mas nmr study of the structure of calcium silicate hydrate, Advanced Cement Based Materials 3 (3) (1996) 144–156.

[36] E. Pustovgar, R. P. Sangodkar, A. S. Andreev, M. Palacios, B. F. Chmelka, R. J. Flatt, J.-B. d. de Lacaillerie, Understanding silicate hydration from quantitative analyses of hydrating tricalcium silicates, Nature communications 7 (2016) 10952.

[37] I. Richardson, Tobermorite/jennite-and tobermorite/calcium hydroxide-based models for the structure of csh: applicability to hardened pastes of tricalcium silicate, β-dicalcium silicate, portland cement, and blends of portland cement with blast-furnace slag, metakaolin, or silica fume, Cement and Concrete Research 34 (9) (2004) 1733–1777.

[38] S. Merlino, E. Bonaccorsi, T. Armbruster, The real structure of tobermorite 11å normal and anomalous forms, od character and polytypic modifications, European Journal of Mineralogy 13 (3) (2001) 577–590.

[39] G. Kovačević, B. Persson, L. Nicoleau, A. Nonat, V. Veryazov, Atomistic modeling of crystal structure of ca1. 67sihx, Cement and concrete research 67 (2015) 197–203.

[40] L. Martínez, R. Andrade, E. G. Birgin, J. M. Martínez, Packmol: a package for building initial configurations for molecular dynamics simulations, Journal of computational chemistry 30 (13) (2009) 2157–2164.

[41] S. M. Mutisya, C. R. Miranda, The surface stability and morphology of tobermorite 11 å from first principles, Applied Surface Science 444 (2018) 287–292.

[42] R. K. Mishra, A. K. Mohamed, D. Geissbühler, H. Manzano, T. Jamil, R. Shahsavari, A. G. Kalinichev, S. Galmarini, L. Tao, H. Heinz, P. Roland, A. C. T. van Duin, S. C. Parker, R. J. Flatt, P. Bowen, cemff: A force field database for cementitious materials including validations, applications and opportunities, Cement and Concrete Research 102 (2017) 68–89.

[43] S. Plimpton, Fast parallel algorithms for short-range molecular dynamics, Journal of computational physics 117 (1) (1995) 1–19.

[44] J. A. Greathouse, J. S. Durkin, J. P. Larentzos, R. T. Cygan, Implementation of a morse potential to model hydroxyl behavior in phyllosilicates, The Journal of chemical physics 130 (13) (2009) 134713.

[45] M. Pouvreau, J. A. Greathouse, R. T. Cygan, A. G. Kalinichev, Structure of hydrated gibbsite and brucite edge surfaces: Dft results and further development of the clayff classical force field with metal–o–h angle bending terms, The Journal of Physical Chemistry C 121 (27) (2017) 14757–14771.

[46] M. Pouvreau, J. A. Greathouse, R. T. Cygan, A. G. Kalinichev, Structure of hydrated kaolinite edge surfaces: Dft results and further development of the clayff classical force field with metal–o–h angle bending terms, The Journal of Physical Chemistry C 123 (18) (2019) 11628–11638.

[47] O. Teleman, B. Jönsson, S. Engström, A molecular dynamics simulation of a water model with intramolecular degrees of freedom, Molecular Physics 60 (1) (1987) 193–203.

[48] R. W. Hockney, J. W. Eastwood, Computer simulation using particles, CRC Press, 1988.

[49] J. P. Larentzos, J. A. Greathouse, R. T. Cygan, An ab initio and classical molecular dynamics investigation of the structural and vibrational properties of talc and pyrophyllite, The Journal of Physical Chemistry C 111 (34) (2007) 12752–12759.

[50] M. P. Allen, D. J. Tildesley, Computer simulation of liquids, Oxford university press, 1989.

[51] P. Liu, E. Harder, B. Berne, On the calculation of diffusion coefficients in confined fluids and interfaces with an application to the liquid-vapor interface of water, The Journal of Physical Chemistry B 108 (21) (2004) 6595–6602.

[52] Y. He, K.-i. Nomura, R. K. Kalia, A. Nakano, P. Vashishta, Structure and dynamics of water confined in nanoporous carbon, Physical Review Materials 2 (11) (2018) 115605.

[53] A. Shekhar, R. K. Kalia, A. Nakano, P. Vashishta, C. K. Alm, A. Malthe-Sørenssen, Universal stretched exponential relaxation in nanoconfined water, Applied Physics Letters 105 (16) (2014) 161907.

[54] N. Bloembergen, E. M. Purcell, R. V. Pound, Relaxation effects in nuclear magnetic resonance absorption, Physical review 73 (7) (1948) 679.

[55] R. Kimmich, Principles of soft-matter dynamics: Basic theories, non-invasive methods, mesoscopic aspects, Springer Science & Business Media, 2012.

[56] M. Youssef, R. J.-M. Pellenq, B. Yildiz, Glassy nature of water in an ultraconfining disordered material: the case of calcium- silicate- hydrate, Journal of the American Chemical Society 133 (8) (2011) 2499–2510.

[57] S. H. Lee, P. J. Rossky, A comparison of the structure and dynamics of liquid water at hydrophobic and hydrophilic surfaces—a molecular dynamics simulation study, The Journal of chemical physics 100 (4) (1994) 3334–3345.

[58] S. M. Mutisya, A. Kirch, J. M. de Almeida, V. M. Sánchez, C. R. Miranda, Molecular dynamics simulations of water confined in calcite slit pores: An nmr spin relaxation and hydrogen bond analysis, The Journal of Physical Chemistry C 121 (12) (2017) 6674–6684.

[59] A. Kirch, S. M. Mutisya, V. M. Sánchez, J. M. de Almeida, C. R. Miranda, A fresh molecular look at calcite-brine nanoconfined interfaces, The Journal of Physical Chemistry C 122 (11) (2018) 6117–6127.

[60] D. Hou, Z. Li, Molecular dynamics study of water and ions transport in nano-pore of layered structure: A case study of tobermorite, Microporous and mesoporous materials 195 (2014) 9–20.

[61] A. Muller, K. Scrivener, A. Gajewicz, P. McDonald, Use of bench-top nmr to measure the density, composition and desorption isotherm of c–s–h in cement paste, Microporous and Mesoporous Materials 178 (2013) 99–103.

[62] M.-C. Bellissent-Funel, S. Chen, J.-M. Zanotti, Single-particle dynamics of water molecules in confined space, Physical Review E 51 (5) (1995) 4558.

[63] K. Amann-Winkel, M.-C. Bellissent-Funel, L. E. Bove, T. Loerting, A. Nilsson, A. Paciaroni, D. Schlesinger, L. Skinner, X-ray and neutron scattering of water, Chemical reviews 116 (13) (2016) 7570–7589.

[64] S. Chen, C. Liao, F. Sciortino, P. Gallo, P. Tartaglia, Model for single-particle dynamics in supercooled water, Physical Review E 59 (6) (1999) 6708.

[65] A. Faraone, E. Fratini, P. Baglioni, S.-H. Chen, Quasielastic and inelastic neutron scattering on hydrated calcium silicate pastes, The Journal of chemical physics 121 (7) (2004) 3212–3220.

[66] A. Lerbret, A. Hédoux, B. Annighöfer, M.-C. Bellissent-Funel, Influence of pressure on the low-frequency vibrational modes of lysozyme and water: A complementary inelastic neutron scattering and molecular dynamics simulation study, Proteins: Structure, Function, and Bioinformatics 81 (2) (2013) 326–340.

[67] R. T. Cygan, L. L. Daemen, A. G. Ilgen, J. L. Krumhansl, T. M. Nenoff, Inelastic neutron scattering and molecular simulation of the dynamics of interlayer water in smectite clay minerals, The Journal of Physical Chemistry C 119 (50) (2015) 28005–28019.

[68] N. W. Ockwig, R. T. Cygan, L. J. Criscenti, T. M. Nenoff, Molecular dynamics studies of nanoconfined water in clinoptilolite and heulandite zeolites, Physical Chemistry Chemical Physics 10 (6) (2008) 800–807.

[69] N. W. Ockwig, R. T. Cygan, M. A. Hartl, L. L. Daemen, T. M. Nenoff, Incoherent inelastic neutron scattering studies of nanoconfined water in clinoptilolite and heulandite zeolites, The Journal of Physical Chemistry C 112 (35) (2008) 13629–13634.

[70] C. Corsaro, V. Crupi, D. Majolino, S. F. Parker, V. Venuti, U. Wanderlingh, Inelastic neutron scattering study of water in hydrated lta-type zeolites, The Journal of Physical Chemistry A 110 (3) (2006) 1190–1195.

[71] D. Eisenberg, W. Kauzmann, The structure and properties of water, Oxford University Press on Demand, 2005.

[72] W. Kob, Computer simulations of supercooled liquids and glasses, Journal of Physics: Condensed Matter 11 (10) (1999) R85–R115.

[73] A. Roder, W. Kob, K. Binder, Structure and dynamics of amorphous silica surfaces, The Journal of Chemical Physics 114 (17) (2001) 7602–7614.

[74] M. J. A. Qomi, M. Bauchy, F.-J. Ulm, R. J.-M. Pellenq, Anomalous composition-dependent dynamics of nanoconfined water in the interlayer of disordered calcium-silicates, The Journal of chemical physics 140 (5) (2014) 054515.

[75] A. Mitzithras, J. H. Strange, Diffusion of fluids in confined geometry, Magnetic resonance imaging 12 (2) (1994) 261–263.

[76] L. Bocquet, J.-L. Barrat, Diffusive motion in confined fluids: Mode-coupling results and molecular-dynamics calculations, EPL (Europhysics Letters) 31 (8) (1995) 455.

[77] H. N. Bordallo, L. P. Aldridge, P. Fouquet, L. C. Pardo, T. Unruh, J. Wuttke, F. Yokaichiya, Hindered water motions in hardened cement pastes investigated over broad time and length scales, ACS Applied Materials & Interfaces 1 (10) (2009) 2154–2162.

[78] J. S. Bhatt, P. J. McDonald, D. A. Faux, N. C. Howlett, S. V. Churakov, Nmr relaxation parameters from molecular simulations of hydrated inorganic nanopores, International Journal of Quantum Chemistry 114 (18) (2014) 1220–1228.

[79] W. Kagunya, P. Dutta, Z. Lei, Dynamics of water in hydrotalcite, Physica B: Condensed Matter 234 (1997) 910–913.

[80] A. G. Kalinichev, R. J. Kirkpatrick, R. T. Cygan, Molecular modeling of the structure and dynamics of the interlayer and surface species of mixed-metal layered hydroxides: chloride and water in hydrocalumite (friedel's salt), American Mineralogist 85 (7-8) (2000) 1046–1052.

[81] A. G. Kalinichev, R. J. Kirkpatrick, Molecular dynamics modeling of chloride binding to the surfaces of calcium hydroxide, hydrated calcium aluminate, and calcium silicate phases, Chemistry of Materials 14 (8) (2002) 3539–3549.

[82] K. S. Smirnov, D. Bougeard, A molecular dynamics study of structure and short-time dynamics of water in kaolinite, The Journal of Physical Chemistry B 103 (25) (1999) 5266–5273.

[83] J. A. Greathouse, K. Refson, G. Sposito, Molecular dynamics simulation of water mobility in magnesium-smectite hydrates, Journal of the American Chemical Society 122 (46) (2000) 11459–11464.

[84] A. Faraone, S.-H. Chen, E. Fratini, P. Baglioni, L. Liu, C. Brown, Rotational dynamics of hydration water in dicalcium silicate by quasielastic neutron scattering, Physical Review E 65 (4) (2002) 040501.

[85] H. Bakker, S. Woutersen, H.-K. Nienhuys, Reorientational motion and hydrogen-bond stretching dynamics in liquid water, Chemical Physics 258 (2) (2000) 233–245.

[86] A. C. Fogarty, F.-X. Coudert, A. Boutin, D. Laage, Reorientational dynamics of water confined in zeolites, ChemPhysChem 15 (3) (2014) 521–529.

[87] A. A. Milischuk, B. M. Ladanyi, Structure and dynamics of water confined in silica nanopores, The Journal of chemical physics 135 (17) (2011) 174709.

[88] J. White, Diffusion of water in li-montmorillonite studied by quasielastic neutron scattering, Clays and Clay Minerals 29 (4) (1981) 241–248.

[89] D. A. Faux, P. J. McDonald, Explicit calculation of nuclear-magnetic-resonance relaxation rates in small pores to elucidate molecular-scale fluid dynamics, Physical Review E 95 (3) (2017) 033117.

[90] D. Laage, J. T. Hynes, On the molecular mechanism of water reorientation, The Journal of Physical Chemistry B 112 (45) (2008) 14230–14242.

[91] D. Laage, J. T. Hynes, A molecular jump mechanism of water reorientation, Science 311 (5762) (2006) 832–835.

[92] R. Blinc, M. Burgar, G. Lahajnar, M. Rožmarin, V. Rutar, I. Kocuvan, J. UršIč, Nmr relaxation study of adsorbed water in cement and c3s pastes, Journal of the American Ceramic Society 61 (1-2) (1978) 35–37.

[93] J.-P. Korb, M. Whaley-Hodges, R. Bryant, Translational diffusion of liquids at surfaces of microporous materials: Theoretical analysis of field-cycling magnetic relaxation measurements, Physical Review E 56 (2) (1997) 1934.

[94] K. R. Brownstein, C. Tarr, Importance of classical diffusion in nmr studies of water in biological cells, Physical Review A 19 (6) (1979) 2446.

[95] L. Schreiner, J. Mactavish, L. Miljković, M. Pintar, R. Blinc, G. Lahajnar, D. Lasic, L. Reeves, Nmr line shape-spin-lattice relaxation correlation study of portland cement hydration, Journal of the American Ceramic Society 68 (1) (1985) 10–16.

[96] J. Greener, H. Peemoeller, C. Choi, R. Holly, E. J. Reardon, C. M. Hansson, M. M. Pintar, Monitoring of hydration of white cement paste with proton nmr spin–spin relaxation, Journal of the American Ceramic Society 83 (3) (2000) 623–627.

[97] R. Holly, E. Reardon, C. Hansson, H. Peemoeller, Proton spin–spin relaxation study of the effect of temperature on white cement hydration, Journal of the American Ceramic Society 90 (2) (2007) 570–577.

[98] A. C. Muller, K. L. Scrivener, A. M. Gajewicz, P. J. McDonald, Densification of c–s–h measured by 1h nmr relaxometry, The Journal of Physical Chemistry C 117 (1) (2012) 403–412.

[99] P. McDonald, J.-P. Korb, J. Mitchell, L. Monteilhet, Surface relaxation and chemical exchange in hydrating cement pastes: a two-dimensional nmr relaxation study, Physical Review E 72 (1) (2005) 011409.

[100] P. J. McDonald, J. Mitchell, M. Mulheron, P. S. Aptaker, J.-P. Korb, L. Monteilhet, Two-dimensional correlation relaxometry studies of cement

pastes performed using a new one-sided nmr magnet, Cement and concrete research 37 (3) (2007) 303–309.

[101] M. N. d'Eurydice, E. T. Montrazi, C. A. Fortulan, T. J. Bonagamba, T2-filtered t2- t2 exchange nmr, The Journal of chemical physics 144 (20) (2016) 204201.

[102] R. Feldman, P. Sereda, A new model for hydrated portland cement and its practical implications, Engineering Journal 53 (8/9) (1970) 53–59.

[103] R. F. Feldman, P. J. Sereda, A model for hydrated portland cement paste as deduced from sorption-length change and mechanical properties, Materials and structures 1 (6) (1968) 509–520.

[104] R. F. Feldman, The flow of helium into the interlayer spaces of hydrated portland cement paste, Cement and Concrete Research 1 (3) (1971) 285–300.